buildings

MDPI

Article

Mechanical, Chloride Permeation, and Freeze–Thaw Resistance of Recycled Micronized Powder Polypropylene-Fiber-Engineered Cementitious Composites

Lei Zheng and Jinzhi Zhou *

School of Civil Engineering, Architecture and Environment, Hubei University of Technology, Wuhan 430068, China; 102110953@hbut.edu.cn
* Correspondence: zhoujinzhi@hbut.edu.cn

Abstract: Research on engineered cementitious composites was carried out using recycled micronized powder from waste construction waste as a substitute for cement. Consequently, this paper focuses on the investigation of recycled micronized powder (RMP) as the subject of study. Using RMP-PP-ECCA0 as the control group, we explored the impact of polypropylene fiber content (0.5%, 1%, 1.5%, 2%) and the substitution rate of RMP (10%, 20%, 30%, 40%) on the mechanical properties, resistance to chloride ion penetration, and freeze–thaw durability of recycled micronized powder polypropylene-fiber-engineered cementitious composites (RMP-PP-ECCs). It was found that, with the increase in RMP substitution rate and fiber content, the mechanical, chloride ion permeation, and freeze–thaw resistance of recycled micronized powder polypropylene-fiber-engineered cementitious composites showed a trend of increasing and then decreasing when the RMP substitution rate was 10%, and the fiber content was 1.5%; the compressive, tensile, chloride ion permeation, and freeze–thaw resistance of recycled micronized powder polypropylene-fiber-engineered cementitious composites were most obviously improved. Compressive strength performance increased by 18.8%, tensile strength performance increased by 80.8%, maximum tensile strain increased by 314%, and electrical flux decreased by 56.3%. Meanwhile, when the recycled micronized powder substitution rate was 10%, the fiber content was 1%, with the most obvious improvement in flexural and freeze–thaw cycle resistance, compared with the control group 28 d flexural strength increased by 22%, after 150 freeze–thaw cycles, the mass-loss rate was reduced by 26%, and the relative dynamic elastic modulus was improved by 4%. In addition, the chemical composition of the regenerated microfractions and the defects in the matrix of the fracture surface of the tensile specimens, the distribution of polypropylene fibers, the surface morphology, and the failure mode were analyzed by X-ray diffraction and scanning electron microscopy.

Keywords: recycled micronized powder; polypropylene fiber; engineered cementitious composites; freeze–thaw cycle; chloride ion penetration

Citation: Zheng, L.; Zhou, J. Mechanical, Chloride Permeation, and Freeze–Thaw Resistance of Recycled Micronized Powder Polypropylene-Fiber-Engineered Cementitious Composites. *Buildings* **2023**, *13*, 2755. https://doi.org/10.3390/buildings13112755

Academic Editor: Abdelhafid Khelidj

Received: 1 October 2023
Revised: 24 October 2023
Accepted: 26 October 2023
Published: 31 October 2023

1. Introduction

In the present era, as natural resource depletion continues unabated and climate change becomes increasingly exacerbated, sustainable development has become a topic of great concern [1–5]. The quantity of construction waste is escalating at a rapid pace in tandem with the ongoing advancements in modernization. The total commercial concrete production in China in 2020 reached 2.843 billion m^3. The average recycling rate in China has been less than 10% [6,7], and the indiscriminate disposal of discarded concrete poses a significant environmental burden. Therefore, how to effectively utilize this part of RMP to improve the comprehensive utilization rate of construction waste and reduce its secondary pollution to the environment is a new challenge for the research of construction waste resource utilization [8–14]. In related fields, researchers are actively working on RMP. A company in South Korea used waste concrete for innovation and successfully realized

the production of cement [15]. Kim et al. [16] also used waste concrete powder to replace traditional silicate cement for concrete preparation, demonstrating the potential feasibility and value. Zhang [17] investigated the activation effect of different activation methods on recycled concrete powder (RCP).

Due to the large particle size, irregular particle shape, and loose texture of RCP, the mixing water requirement of ECCs is significantly higher than that of ordinary engineered cementitious composites (ECCs) at a higher substitution rate, which leads to the low mechanical, chlorine ion infiltration resistance and frost resistance properties of ECCs. Tang et al. [18] found that the fineness of RMP had a significant effect on concrete properties. RMP with finer particles favored the mechanical properties of concrete. The durability of concrete was improved when the fineness of RMP was better than the fineness of cement. For this reason, the author used crusher and planetary ball mill for crushing and fine grinding of concrete construction waste, the average diameter of which was controlled to be below 3.63 μm. Due to its small particle size, it can play the role of micro-aggregate filling effect and enhance the compactness of recycled micronized powder polypropylene-fiber-engineered cementitious composites (RMP-PP-ECCs), and by utilizing the characteristics of RMP, it can be used to partially replace cement in the preparation of RMP-PP-ECCs, which is not only to reduce the dosage of cement to lower the cost but also important for low-carbon and environmental protection. It not only reduces the amount of cement and cost but also has an important significance for low-carbon and environmental protection [19–23].

Currently, the main types of fibers used in reinforcement materials are steel fibers, polyvinyl alcohol fibers, polyethylene fibers, and polypropylene (PP) fibers. Among these options, PP fibers offer several advantages. It significantly improves bonding and friction with cementitious materials, thereby improving performance after cracking, and PP fibers exhibit superior corrosion resistance compared to steel fibers. Compared to polyvinyl alcohol fibers and polyvinyl alcohol fibers, PP fibers are easier to process, less expensive and easier to disperse, and are also safe and environmentally friendly. At present, the combination of fibers and recycled coarse and fine aggregate concrete to improve the performance of concrete has achieved more results, while the use of fibers to improve the performance of ECCs is relatively weak [24,25]; on the other hand, countries around the world have mainly studied the expensive polyethylene and polyvinyl alcohol long fibers (12–36 mm) to enhance the mechanical and ductile aspects of RMP-PP-ECCs [26,27]. Short-cut PP is a high-quality, inexpensive, and easily dispersible cement mortar and concrete reinforcing fiber; the technology in question has gained widespread usage across multiple engineering disciplines and holds significant research value. Furthermore, the addition of PP has the potential to greatly enhance the mechanics, frost resistance, chloride permeability, and ductility of RMP-PP-ECCs [28–32], thus improving the safety of the structure, so this paper explores the effects of different RMP substitution rates and different polypropylene short-cut fiber incorporation amounts on the mechanical and durability properties of RMP-PP-ECCs after mechanical activation.

2. Experimental Preparation

2.1. Materials

In this experiment, P.O42.5 ordinary silicate cement produced by Wuhan Yadong Cement Co., Ltd. (Wuhan, China) was used, as well as first-grade fly ash and high-quality silica fume. Table 1 lists the chemical composition of the cementitious materials, as determined by X-ray fluorescence (XRF) testing. PP fiber was provided by "Huixiang Fiber Production Plant". PP fiber is shown in Figure 1; Table 2 shows the physical properties of PP fiber.

Table 1. Chemical compositions of cementitious materials (%).

Material	CaO	SiO_2	Fe_2O_3	Al_2O_3	SO_3	K_2O	MgO	TiO_2	Na_2O
Cement	48.56	26.54	3.44	12.45	4.87	0.67	2.45	0.67	0.35
RMP	42.54	25.34	2.35	5.54	0.87	1.26	2.64	0.32	0.65
Fly ash	1.47	54.07	4.01	26.83	0.85	1.54	1.36	1.56	0.54
Silica fume	0.23	94.35	0.21	0.21	0.32	0.21	0.41	0.11	0.15

Figure 1. PP fiber.

Table 2. Physical properties of PP fiber.

Fiber Type	Density ($kg \cdot m^{-3}$)	Tensile Strength (MPa)	Elongation at Break (%)	Length (mm)	Moisture Content (%)	Young's Modulus (GPa)	Diameter (μm)
PP	910	350	35	6	2	3.5	35

2.2. RMP Preparation Process

The research material of RMP used in this study originated from a construction site in the Wuhan area, which was initially waste concrete. The original strength grade of this concrete was C45. In the treatment process, a jaw crusher was used for the initial crushing of the construction waste, followed by exposure to sunlight and drying, and then process steps such as screening and ball milling, which ultimately formed the RMP material used in this study, Figure 2 shows the specific production process.

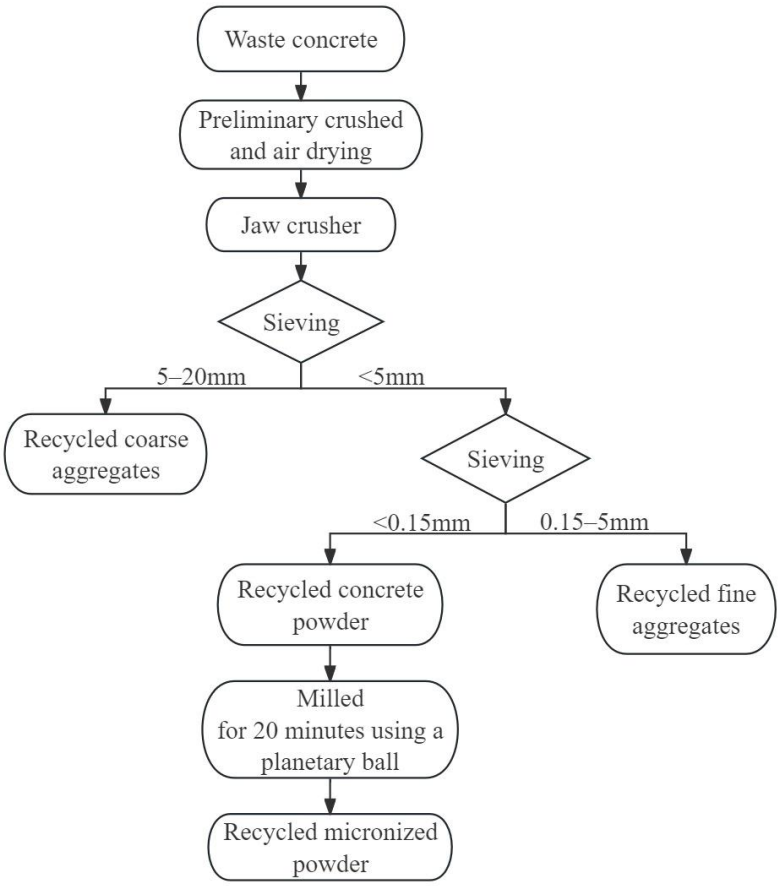

(**a**) RMP processing

(**b**) Planetary ball mills

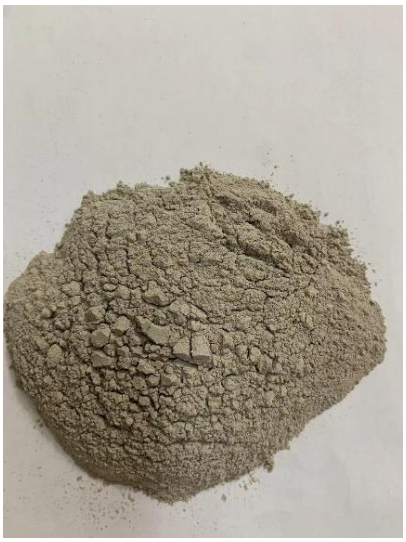

(**c**) RMP

Figure 2. Production process of RMP.

2.3. RMP-PP-ECC Mixing Ratio Design

The experimental mixing ratios are shown in Table 3. This experiment investigated the effect of the RMP substitution rate and the PP volume content in RMP-PP-ECCs on their compressive strength, uniaxial tensile strength, and flexural strength. The compressive strength was tested using a 70.5 mm × 70.5 mm × 70.5 mm cube specimen, the flexural strength was tested using a 40 mm × 40 mm × 160 mm specimen, and the uniaxial tensile strength was tested using a dog-bone-shaped specimen with a cross-sectional area of 14 mm × 30 mm as shown in

Figure 3. The mechanical properties of the three specimens were tested after 7 and 28 d of curing in the curing room. The anti-chlorine ion penetration test was carried out using cylindrical specimens with a diameter of 100 mm at the base and a height of 50 mm, and the frost resistance test was carried out using 100 mm × 100 mm × 400 mm RMP-PP-ECC specimens cast and molded for 24 h. After 24 h of molding and curing in the curing room (temperature (21 ± 1) °C, humidity of 96%) for 28 d, subsequent resistance to chlorine penetration and anti-freezing performance tests were conducted.

Table 3. RMP-PP-ECC mix ratio design.

Mixture	Cement (g)	RMP (g)	Fly Ash (g)	Silica Fume (g)	Sand (g)	PP Fiber (%)	Water (g)	EWR (g)
RMP-PP-ECCA	800	0	100	100	1000	0	250	29
RMP-PP-ECCB0	720	80	100	100	1000	0	250	29
RMP-PP-ECCB0.5	720	80	100	100	1000	0.5	250	29.5
RMP-PP-ECCB1	720	80	100	100	1000	1	250	30
RMP-PP-ECCB1.5	720	80	100	100	1000	1.5	250	31
RMP-PP-ECCB2	720	80	100	100	1000	2	250	31.5
RMP-PP-ECCC0	640	160	100	100	1000	0	250	29
RMP-PP-ECCC0.5	640	160	100	100	1000	0.5	250	29.5
RMP-PP-ECCC1	640	160	100	100	1000	1	250	30
RMP-PP-ECCC1.5	640	160	100	100	1000	1.5	250	31
RMP-PP-ECCC2	640	160	100	100	1000	2	250	31.5
RMP-PP-ECCD0	560	240	100	100	1000	0	250	29
RMP-PP-ECCD0.5	560	240	100	100	1000	0.5	250	29.5
RMP-PP-ECCD1	560	240	100	100	1000	1	250	30
RMP-PP-ECCD1.5	560	240	100	100	1000	1.5	250	31
RMP-PP-ECCD2	560	240	100	100	1000	2	250	31.5
RMP-PP-ECCE0	480	320	100	100	1000	0	250	29
RMP-PP-ECCE0.5	480	320	100	100	1000	0.5	250	29.5
RMP-PP-ECCE1	480	320	100	100	1000	1	250	30
RMP-PP-ECCE1.5	480	320	100	100	1000	1.5	250	31
RMP-PP-ECCE2	480	320	100	100	1000	2	250	31.5

Note: EWR means efficient water reducer.

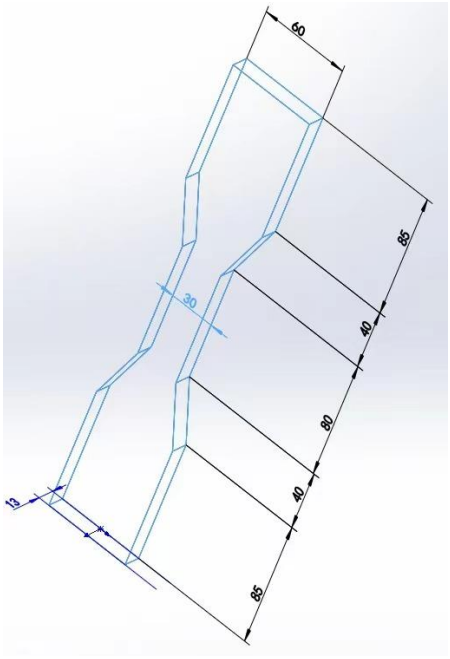

Figure 3. RMP-PP-ECC tensile test.

2.4. Microstructural Test

The particle sizes of the four cementitious materials were determined utilizing a laser particle size analyzer, as shown in Figure 4. The average particle sizes of cement, fly ash, RMP, and silica fume are 12.74 μm, 12.86 μm, 3.63 μm, and 2.85 μm, respectively. An eight-channel TAM Air microtester from TAM Instruments was used to determine the exothermic rate and the effect of exotherm on the hydration of RMP and recycled micronized cementitious systems from 0 to 3 d at 20 °C. The exothermic rate of RMP and recycled micronized cementitious systems was determined by using an eight-channel TAM Air microtester. The mass of cementitious material used in the test was 5 g, the water–cement ratio was 0.25, and the test temperature was 22 °C. The four cementitious materials were scanned by an X-ray diffraction (XRD) analyzer, and the specimens were subjected to vacuum drying at 50 °C for a duration of 48 h within a vacuum drying oven. Afterward, the specimens were pulverized with a mortar, and the pulverized samples were passed through a 75 μm round hole sieve and then placed in a drying oven to preserve. In addition, the micro-morphology of the fracture surface of the specimens after tensile damage was observed by scanning electron microscope (SEM). The microscopic mechanism of the effect of recycled micronized powders and fibers on the mechanical properties of cementitious materials was investigated. The drying process was carried out in a vacuum drying oven at a temperature of 50 °C for 1 h and subsequently placed in a drying oven for storage. The middle part of each sample was used as a preserved specimen and coated with a gold film. In order to observe the microstructural changes on the fracture surfaces of the tensile specimens after failure, RMP-PP-ECCB1.5, RMP-PP-ECCC1.5, RMP-PP-ECCD1.5, and RMP-PP-ECCE1.5 tensile specimens were selected and observed and analyzed using a Hitachi S-3400N scanning electron microscope (SEM).

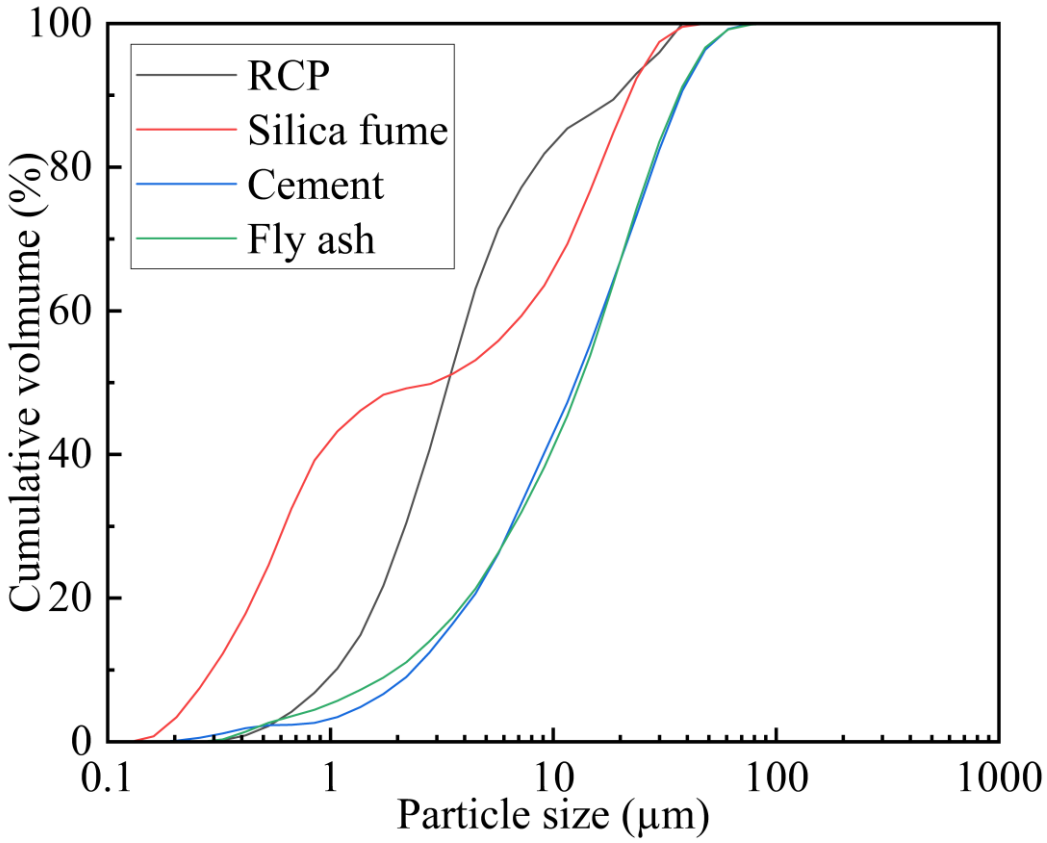

Figure 4. Particle size distributions for cementitious materials.

2.5. Methodology of the Experiment and the System for Applying Loads

The mechanical property test refers to GB/T 50081-2019 [33]. The compressive strength and flexural strength tests were carried out by a DYE-300S microcomputer servo cement flexural and compressive testing machine produced Cangzhou Zhulong Engineering Instrument Co. (Changzhou, China). The loading rate controlled by stress was 0.5 MPa/s in the compressive test and 50.0 N/s in the flexural test using a WDW-100C microcomputer-controlled electronic universal testing machine. The electronic universal testing machine was used for the tensile test, the loading rate controlled by displacement was 0.4 mm/min, and the strain of the specimen was measured by an electronic extensometer with a scale distance of 50 mm. The uniaxial tensile test is a common method in the mechanical testing of materials. When performing uniaxial tensile tests, we need to measure mechanical parameters such as stress and strain. For this purpose, we used the method of dividing the tensile force by the cross-sectional area to calculate the stress and dividing the elongation by the scale distance to calculate the strain. The compressive strength and flexural strength were tested after 7 and 28 d. The tensile strength tests were conducted with 3 specimens each. In the end, we take the average of the test results of the three specimens as the final test results and analyze and compare the data. In this way, we can obtain the mechanical property data of the material under uniaxial tensile conditions, which can offer foundational data support for future research and practical applications.

2.6. Chloride Ion Permeability Testing

The resistance to chloride ion penetration test refers to the electric flux method in GB/T 50082-2009 [34], which records the passing flux. The electric flux test was carried out using a multifunctional concrete durability synthesizer, as shown in Figure 5. The current is recorded every 5 min through the automatic data collection function until it reaches 6 h. The current versus time is plotted according to the recorded data, and the area integral of the curve is used to obtain the electric flux (C) of the test for 6 h. Finally, the calculated electric flux is converted into the electric flux of the specimen with a diameter of 95 mm according to the following formula. As shown in Equation (1):

$$Qs = Q_x \times (95 \div x)^2 \quad (1)$$

where Qs is the electric flux (C) through a specimen with a diameter of 95 mm, and Q_x is the electric flux through a specimen with a diameter of x mm.

Figure 5. Test image of electric flux method.

2.7. Freeze–Thaw Cycle Resistance Test

Referring to GB/T 50082-2009 "Spleted, we quickly put the specimen into the freeze–thaw tester again for another round of freeze–thaw cycles until the specimen reaches the maximum limit value of freeze–thaw cycle resistance. It is important to note that the mass-loss rate of the test specimen is calculated by the Standard for "Test Methods of Long-Term Performance and Durability of Ordinary Concrete" for the freezing resistance

test of RMP-PP-ECC, as shown in Figure 6. By using the fast-freezing method, after 28 days of curing, we put the RMP-PP-ECC into the freeze–thaw testing machine. The cycling temperature interval was set from −18 °C to 8 °C while ensuring that the water surface exceeded the specimen surface by 5 cm. This was achieved by allowing the specimen to warm from −18 °C to 8 °C in 1 h, followed by cooling from 8 °C to −18 °C in 1 h to complete 150 freeze–thaw cycles. Every 25 freeze–thaw cycles, the RMP-PP-ECC specimens were removed, the specimen surfaces were cleaned and dried, and then tested for quality. After the test, its mass change is measured at the conclusion of each measurement, and the test is considered complete when the specimen's mass-loss rate reaches 5%. The mass-loss rate is computed using the formula described in Equation (2):

$$P = \frac{m_i - m_j}{m_i} \times 100\% \tag{2}$$

where P is the % mass-loss rate after j freeze–thaw cycles; m_i is the mass in kg of the ith freeze–thaw cycle; m_j is the mass in kg of the jth freeze–thaw cycle; and $j > i$.

Figure 6. Images of rapid freeze–thaw experimental method.

The dynamic elastic modulus of RMP-PP-ECC is primarily tested by the dynamic method. The freezing resistance of RMP-PP-ECC can be characterized based on the change in RDEM. The test is terminated when the RDEM of the RMP-PP-ECC specimen falls below 60% of the initial value. Where the dynamic elastic modulus is shown in Equation (3):

$$E_d = 13,244 \times 10^4 \times WL^3 f^2 / a^4 \tag{3}$$

where E_d is the dynamic modulus of elasticity in MPa; W is the mass of the RMP-PP-ECC specimen in kg; L is the length of the RMP-PP-ECC specimen in mm; and f is the fundamental frequency vibration frequency of transverse vibration of the specimen in Hz.

The relative dynamic elastic modulus is calculated as shown in Equation (4):

$$P = f_n^2 / f_0^2 \tag{4}$$

where P is the RDEM of the specimen after n freeze–thaw cycles; f_n is the fundamental frequency of transverse vibration of the specimen after the nth freeze–thaw cycle in Hz; and f_0 is the fundamental frequency of transverse vibration of the specimen before the freeze–thaw cycle in Hz.

3. Analysis of Experimental Phenomena and Results

3.1. Experimental Phenomena of RMP-PP-ECC Damaged by Force

As shown in Figure 7, the compressive specimen without fiber doping is loaded continuously; with the continuous increase in the load, the compressive specimen without fiber group reaches a certain value of the load with a loud bang, and the specimen is directly fractured from the middle or the edge of the specimen, and the powder keeps falling off, which shows obvious brittle characteristics. With the loading of the fiber-reinforced

specimen, a small crack began to appear in the middle or edge of the specimen, and there was a tendency to expand, accompanied by the sound of the fiber being pulled out; the specimen was in outward expansion. With the increasing load, the main crack is formed and cracks upward at the lower edge of the test block, and due to the bridging of the fibers, the test block still maintains good integrity and has obvious ductile damage characteristics. As shown in Figure 8, with the continuous increase in the load, the non-fiber-reinforced flexural specimen suddenly ruptured in the middle of the specimen along the vertical direction when the load reached an ultimate value, showing obvious brittle characteristics. While adding the fiber group to the test, the load continues to increase, and when the load reaches an ultimate value, a crack forms along the lower edge of the middle of the test block, accompanied by the sound of the fiber being pulled out. However, the block still maintains the integrity of the performance of cracking but continuous characteristics, with obvious ductile damage characteristics. As shown in Figure 9, the tensile specimen of the unadulterated fiber group will be suddenly pulled off from the middle once the load reaches a certain value during the process of increasing load. Fiber-doped specimen, the loading of the initial stage in the elastic phase, with the increasing load, in the center of the specimen appeared a crack, accompanied by the sound of the fiber being pulled out. The fiber plays the role of bridging and bearing the load until the load reaches a certain value; then, the specimen will be pulled off, showing ductile damage characteristics.

RMP-PP-ECCA0 RMP-PP-ECCB1.5

Figure 7. Compression damage.

RMP-PP-ECCA0 RMP-PP-ECCB1

Figure 8. Flexural damage.

RMP-PP-ECCA0 RMP-PP-ECCB1.5

Figure 9. Tensile damage.

3.2. Analysis of Experimental Results

3.2.1. Heat of Hydration Analysis of RMP and Recycled Micronized Cementitious Systems

The results of the heat of hydration of RMP and recycled micropowder cementitious system at 72 h are shown in Figure 10; the exothermic rate of RMP-PP-ECC is relatively fast in the first 30 h, and then the exothermic rate gradually becomes slower. The unhydrated cement and silicate hydration products in RMP form a continuous secondary hydration reaction with water, which has a certain hydration activity. Due to the finer fineness of RMP, the specific surface area is larger, so that the cement is more easily contacted with water to produce a hydration reaction, and the exothermic rate and exothermic capacity of RMP are improved for a short period of time with an increase in the substitution rate of RMP, and when the substitution rate of RMP is 10%, the total exothermic capacity is the same as that of RMP-PP-ECC0. When the substitution rate of RMP is 10%, the total exothermic amount is not much different from that of RMP-ECC0; when the substitution rate is more than 10%, the total exothermic amount decreases significantly, which is mainly due to the fact that the increase in the substitution rate of RMP reduces the total reactants, and overall reduces the exothermic amount of the samples, and the exothermic amount decreases gradually with the increase in the substitution rate.

3.2.2. XRD Analysis of Cementitious Materials

The XRD analysis results are shown in Figure 11. According to the results of the XRD analysis, it can be found that the main component of RMP is the sand in the concrete, and the sand in the discarded concrete is the sand. SiO_2 and calcite ($CaCO_3$) are the other two main components of RMP. It is worth noting that calcite has an important role in RMP, which can provide additional hydration sites for cement and thus promote the acceleration of the hydration reaction. At the same time, calcite can also react with hydration products to improve the mechanical properties and durability of RMP-PP-ECC [35]. Large quantities of RMP-PP-ECC containing calcite and dolomite not only enhance the hydration reaction of cement but also effectively fill the inner voids and transition areas between the aggregates, leading to increased concrete density and reduced porosity, thereby greatly enhancing the properties of RMP-PP-ECC [33,36–38]. From the XRD spectra, it can be observed that there are no significant diffraction peaks of $Ca(OH)_2$ and diffraction peaks of calcite in RMP. This is due to the high alkalinity of RMP, which fosters the carbonization of $Ca(OH)_2$, which fosters the carbonization of $Ca(OH)_2$, resulting in relatively low $Ca(OH)_2$

content. Furthermore, the increased surface area of RMP facilitates greater contact between $Ca(OH)_2$ and air, further promoting its carbonization. The diminished $Ca(OH)_2$ content is a consequence of its decomposition caused by the elevated temperature during the RMP milling process. This suggests that after excitation by mechanical ball milling, some of the SiO_2 in the RMP was activated and reacted with the cement's hydration product, $Ca(OH)_2$, in a volcanic ash reaction to produce hydrated calcium silicate. The RMP consists mainly of sand $Ca(OH)_2$ and calcite $CaCO_3$ from natural concrete. Calcite can provide an additional hydration reaction, which is expected to increase the degree of hydration of RMP. In addition, in the XRD spectra, the diffractograms of groups (a)–(d) showed very distinct SiO_2 peaks, with the strongest SiO_2 peak in group (d). The SiO_2 peaks in group d were found in the XRD spectra of RMP. This suggests that the relatively high content of SiO_2 in RMP may be due to the mechanical ball milling excitation that makes SiO_2 activated, which in turn participates in the hydration reaction [39–42].

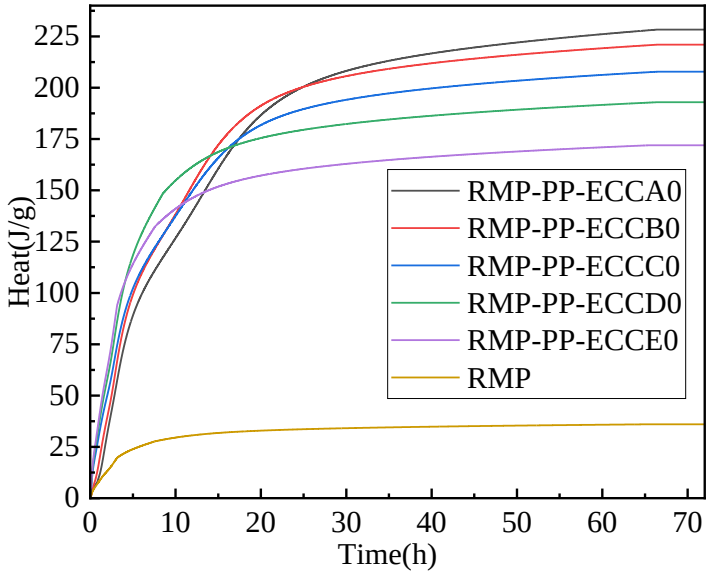

Figure 10. Heat of hydration of RMP and recycled micronized cementitious systems.

3.2.3. Compressive Strength of Cubes

The RMP-PP-ECC specimens were cured according to the schedule for 7 and 28 d, the compressive strength values of the RMP-PP-ECC specimens at each age were determined, and the conclusions were drawn based on Figure 12. The best compressive performance was achieved when the RMP substitution rate was 10% and the PP fiber doped was 1.5%. The 28 d compressive strength increased by 23.7% compared to the 7 d compressive strength. The 28 d compressive strength increased by 18.8% compared to RMP-PP-ECCA0. Due to the high coefficient of friction of PP, they can form a good fiber–cementitious lattice structure in the RMP-PP-ECC, which can carry the loads along with the cementitious matrix. This disordered grid structure can delay the development of internal cracks and enhance the toughness and strength of the RMP-PP-ECC. The experimental results show that the compressive strength of the RMP-PP-ECC reaches the maximum value when the fiber content is 1.5%. In addition, the RMP-PP-ECC was prepared by replacing some of the cement with RMP, the RMP-PP-ECC, which can carry the loads along with the cementitious matrix. This disordered grid structure can delay the development of internal cracks and enhance the toughness and strength of the RMP-PP-ECC. The experimental results show that the compressive strength of the RMP-PP-ECC reaches the maximum value when the fiber content is 1.5%. In addition, the RMP-PP-ECC was prepared by replacing some of the cement with RMP, and it was found that the compressive strength of the RMP-PP-ECC increased slightly when the substitution rate was 10%, but when the substitution rate was more than 10%, the compressive strength of the mortar decreased

at all ages, with the increased water requirement for fluidity being the primary factor contributing to the reduced strength in the RMP-PP-ECC, particularly at lower substitution rates. Conversely, the use of recycled coarse aggregate from waste concrete, with its high alkalinity and alkaline-environment-induced volcanic ash effect, results in the formation of C-S-H gel through chemical reactions. This C-S-H gel effectively fills the internal pores of the RMP-PP-ECC, enhancing its microporous structure. In addition, inactive particles in RMP serve as macroaggregates, filling the cement paste in the matrix. Consequently, lower RMP substitution rates are beneficial for improving the strength of the RMP-PP-ECC. However, when the RMP substitution rate exceeds 10%, it has an adverse effect on the concrete's compressive strength. This adverse impact is attributed to the increased water demand for a specified fluidity. As the RMP substitution rate rises, the cement content in the corresponding RMP-PP-ECC diminishes, leading to a reduction in C-S-H gel content within the hydration products and, consequently, a decline in the strength of the RMP-PP-ECC [43–45].

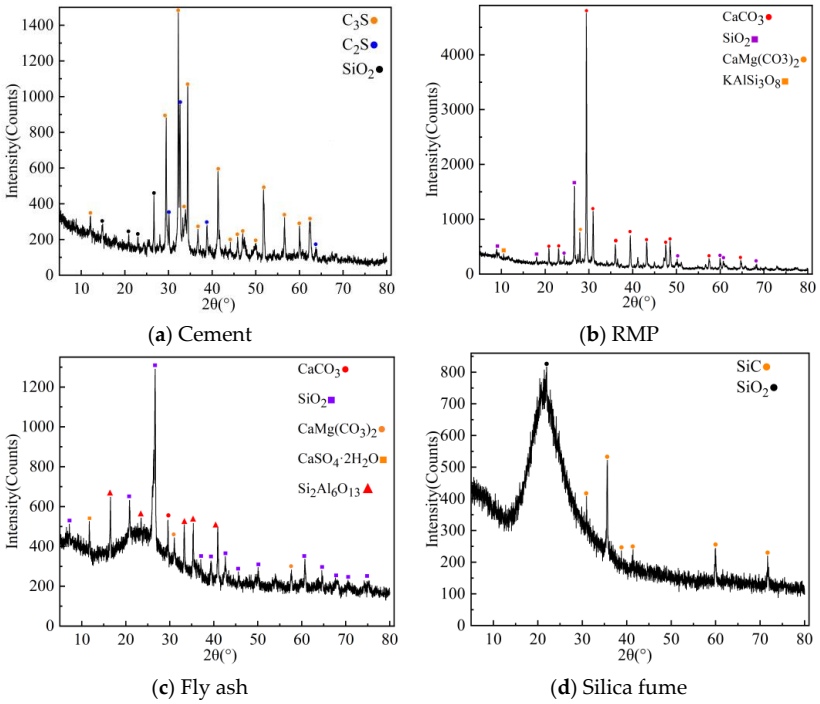

(**a**) Cement (**b**) RMP

(**c**) Fly ash (**d**) Silica fume

Figure 11. The XRD spectra of cementitious materials.

3.2.4. The Flexural Strength of RMP-PP-ECC

The RMP-PP-ECC cubic specimens were cured for 7 and 28 d as per the schedule, and the flexural strength values of the RMP-PP-ECC specimens at each age were determined. According to Figure 13, the best flexural performance is achieved when the RMP substitution rate is 10% and the PP fiber dosage is 1%. According to the results of the described experiments, the 28 d flexural strength increased by 9.1% compared to the 7 d flexural strength; the smaller increase in flexural strength is due to the early hydration reaction leading to the reaction between the RMP and the reactive substances in the cement, and the later hydration reaction generating a lower gel substance, which is able to support the flexural strength of the specimen is reduced is the result. The 28 d flexural strength increased by 22% compared to RMP-PP-ECCA0. In this experiment, the RMP-PP-ECC specimens were subjected to bending moment, while the lower part was subjected to tension, and the fibers showed excellent tensile properties and a bridging effect, which increased the flexural strength of RMP-PP-ECC. The flexural strength of RMP-PP-ECC reaches the maximum value when the fiber content is 1%. When the fiber content exceeds 1%, the internal voids are increased due to the clustering effect of fibers, resulting in a gradual decrease in the

flexural strength of RMP-PP-ECC [46,47]. In addition, when the RMP substitution rate is 10%, the flexural strength of RMP-PP-ECC is slightly increased. However, when the RMP-PP-ECC substitution rate exceeds 10%, the flexural strength of RMP-PP-ECC begins to gradually decrease. This is because the $CaCO_3$ in RMP has a promoting effect on the hydration reaction of cement C_3S and C_3A, and the generated hydration products can form crystal nuclei and increase the C-S-H gel content of the hydration products. At the same time, the unhydrated cement and silicate hydration products in the regenerated micronized powder form a continuous secondary hydration reaction with water, and the slower hydration rate makes the C-S-H gel structure in the interfacial transition zone become denser. The slower hydration rate makes the C-S-H gel structure in the interfacial transition zone become more dense, which improves the flexural strength; however, with the increase in dosage due to the fineness of RMP, the specific surface area is larger, which is easy to lead to an increase in the amount of water required, and the hydration reaction is incomplete, resulting in a decrease in the flexural strength of the cementitious base [48].

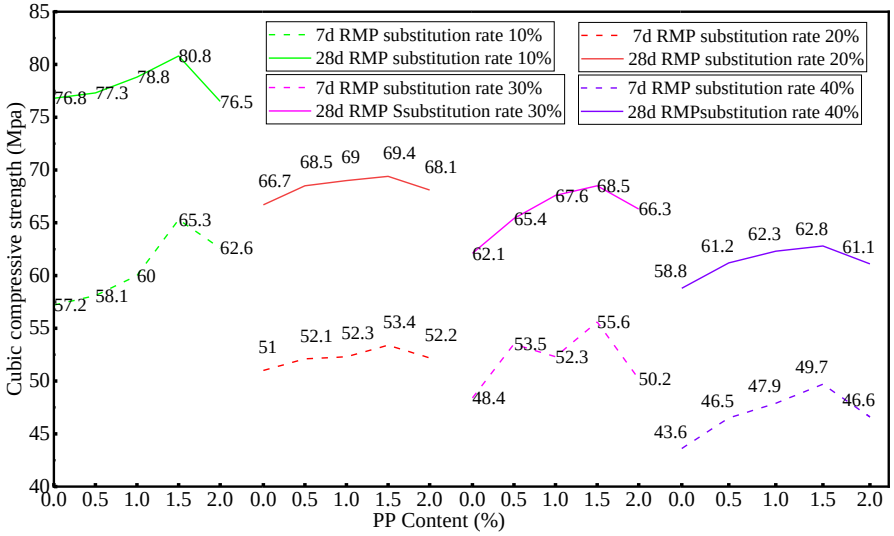

(**a**) RMP-PP-ECCB0-RMP-PP-ECCE2

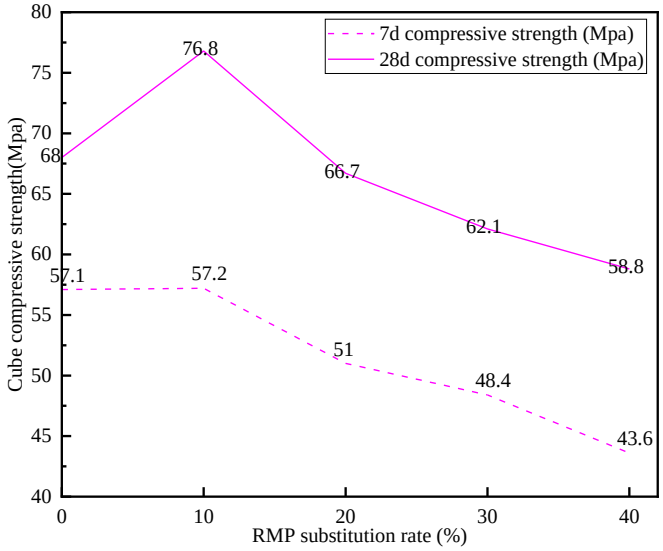

(**b**) Compressive strength of test pieces without fiber group

Figure 12. Cubic compressive strength of RMP-PP-ECCs.

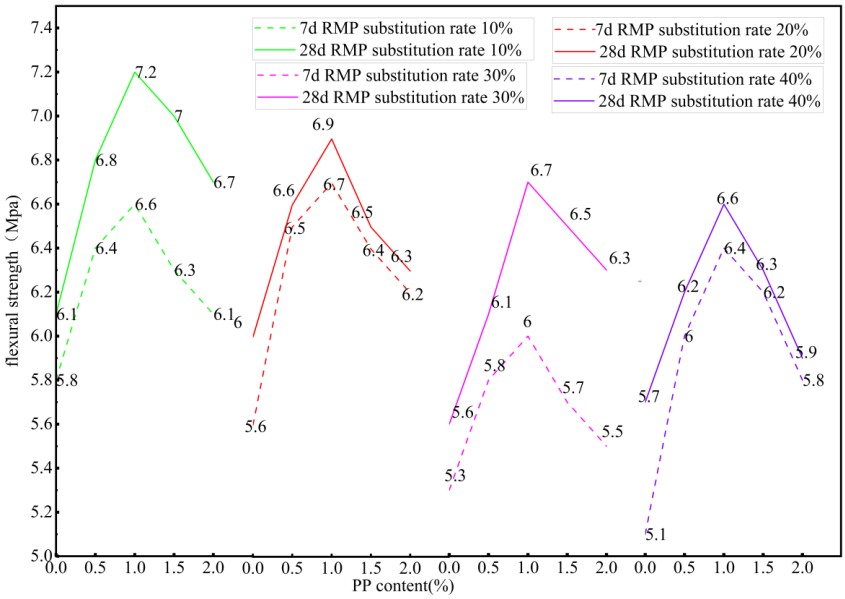

(**a**) RMP-PP-ECCB0-RMP-PP-ECCE2

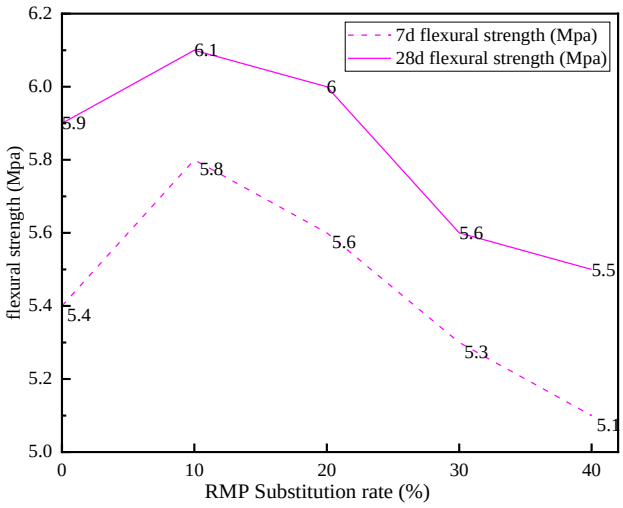

(**b**) Flexural strength of test pieces without fiber group

Figure 13. Flexural strength of RMP-PP-ECCs.

3.2.5. The Tensile Strength of RMP-PP-ECC

The RMP-PP-ECC specimens were cured for 7 and 28 days according to the schedule, and the tensile strength values of RRMP-PP-ECC at each age were determined. According to Figure 14. When the RMP substitution rate is 10%, and the PP fiber doping is 1.5%, the tensile performance is the best, and the 28 d tensile strength increases by 10.2% compared with the 7-day tensile strength. The tensile strength growth is small; the reason is similar to the flexural strength, which is due to the RMP particle size being small while the specific surface area is large. As a result, in the early stage, it can absorb more water for the hydration reaction, generating more gelling material, and the later hydration reaction to generate the gel material is reduced, thus resulting in the late tensile strength growth being slow. The 28 d tensile strength increased by 80.8% compared to RMP-PP-ECCA0. When the RMP-PP-ECC specimen is under the action of tensile force, the fiber plays a good tensile property and bridging role in the process, which makes the tensile strength increase to a certain extent. When the fiber content exceeds 1.5%, the excessive fiber incorporation makes it easy to adhere during the mixing and processing of cementitious materials, the fiber-specific surface area is larger, and the specimen contains more weak layers, which destroys the optimal structure of the specimen, resulting in a reduction in tensile strength.

When the RMP substitution rate is 10%, RMP-PP-ECC has the best tensile performance, and the tensile strength of RMP-PP-ECC is slightly improved compared to ordinary engineered cementitious composites. However, when the RMP substitution rate is more than 10%, the flexural strength of RMP-PP-ECC starts to decrease gradually. The reason is that RMP has a large specific surface area, and the ultrafine powder not only makes the cement better dispersed in the matrix and increases the hydration contact area of the cement but also exposes a part of the unhydrated particles contained in the RMP after deep grinding, which makes the RMP show better hydration activity and improves the tensile strength, but with an increase in the substitution rate of RMP, the RMP absorbs a large amount of water used in the mixing and the amount of water required for the hydration of the cement decreases. The water requirement used for hydration is reduced, leading to the obstruction of cement hydration; on the other hand, the large dosage substitution of cement by RMP leads to the reduction in cement dosage, which reduces the C-S-H content of the hydration products and leads to the reduction in the tensile strength of RMP-PP-ECC [49].

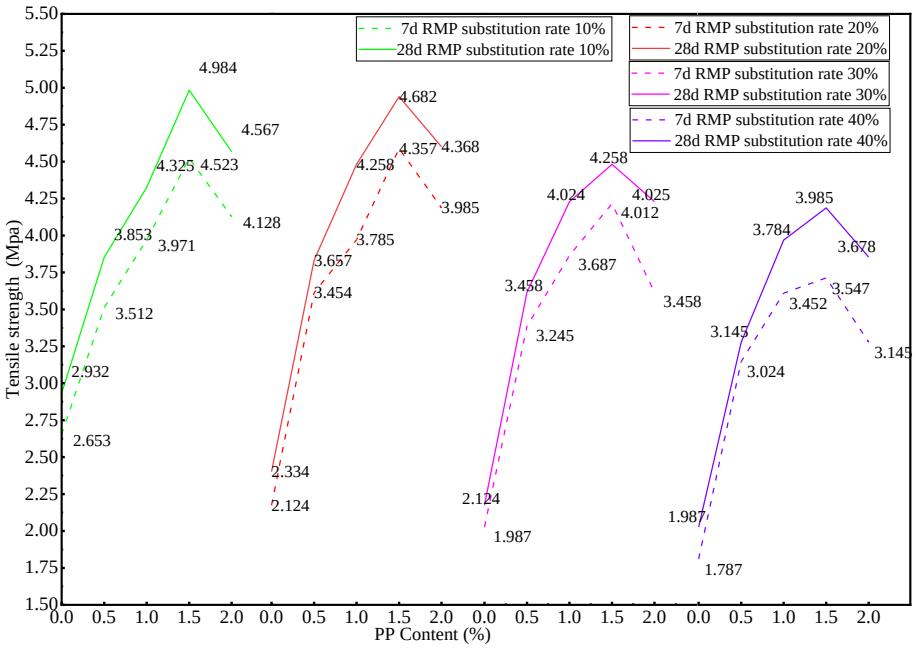

(**a**) RMP-PP-ECCB0-RMP-PP-ECCE2

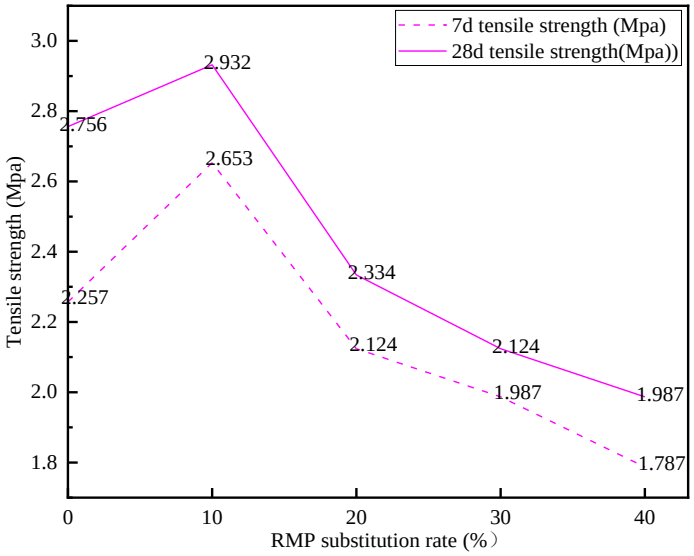

(**b**) Tensile strength of test pieces without fiber group

Figure 14. Tensile strength of RMP-PP-ECC.

3.2.6. Uniaxial Tensile Stress–Strain

A large number of experimental data analyses show that the mechanical properties of RMP-PP-ECC specimens at 7 and 28 d of maintenance with the same rule of change in PP fiber content are limited to space to the maintenance age of 28 d of different PP fiber content. RMP-PP-ECC specimen stress–strain curves are shown as an example in Figure 15. For the unadulterated fiber group, from the starting point of 0, with the increase in load, the strain gradually increases, and the stress–strain is almost a linear elasticity relationship; however, when the load is increased to the limit of the load, the test block suddenly pulls off, resulting in a crack. For the doped fiber group, starting at point 0, with the increase in load, the strain gradually increases; this trend is relatively slow, and at this stage, the predominant form of deformation is primarily elastic in nature, with the load primarily being supported by the cement mortar matrix. The subsequent stage involves the development of internal cracks. Commencing from the initial position of 0 in the fiber-doped test block, as the load is progressively increased, the strain exhibits a gradual increment. This progression is characterized by a relatively slow rate. During this stage, the deformation primarily manifests in an elastic manner, with the load primarily being sustained by the cement mortar matrix. Subsequently, the second stage ensues, marked by the propagation of internal cracks. During this stage, the concrete undergoes a transition from elastic to plastic behavior, as evidenced by an increasing slope of the curve. Additionally, the initiation of interior cracks can be observed. During this particular moment, the initial fracture becomes visible, and the load is shared by both the cementitious materials and fibers in unison.

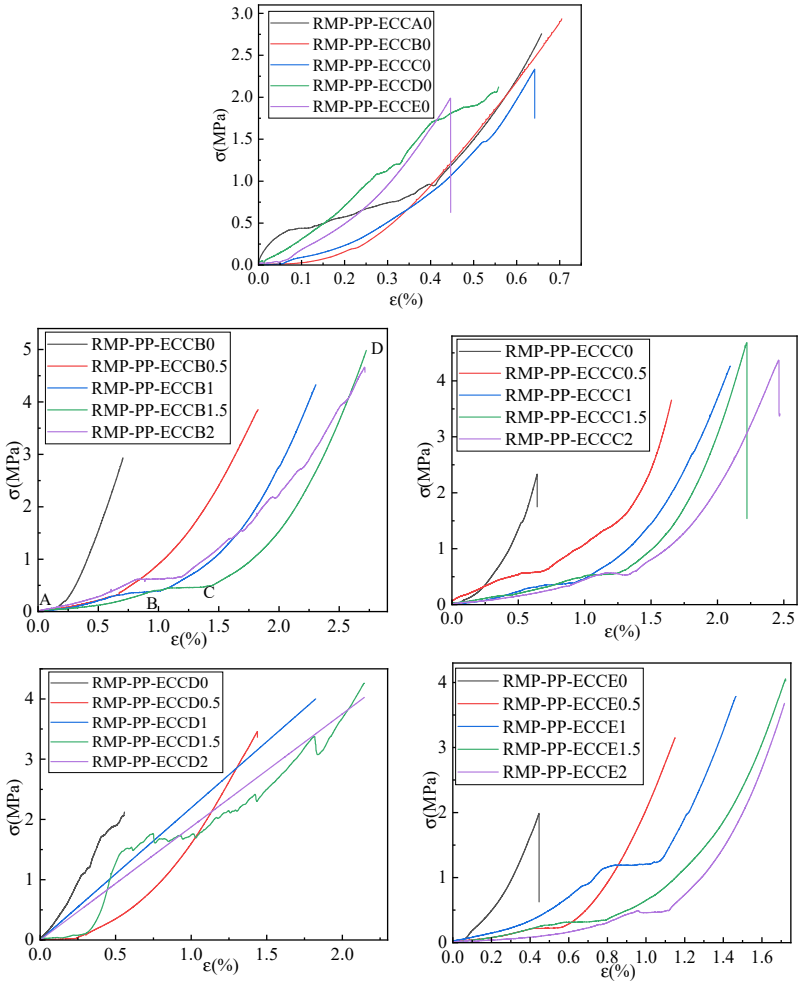

Figure 15. Uniaxial tensile stress–strain curves of RMP-PP-ECCs.

3.2.7. Uniaxial Strength Analysis

The uniaxial tensile and compressive strength ratios of the material can be used as the main index for evaluating the mechanical properties of PP-ECC, and usually, a high tensile and compressive strength ratio prevents the premature generation of longitudinal cracks, but there is no unified research study on the relationship between the tensile strength and the compressive strength of PP-ECC. In this study, based on the tensile test results, the relationship between the compressive strength ($f_{cu70.7}$) and the tensile strength (f_{tp}) of PP-ECC with an edge length of 70.7 mm is obtained, as shown in Figure 16. The relationship between PP-ECC (f_{tp}) and uniaxial compressive strength ($f_{cu70.7}$) was obtained using data fitting as follows:

$$f_{tp} = \frac{94.20176}{1 + e^{\frac{f_{tp}70.7 + 3.79717}{15.12741}}} \quad (5)$$

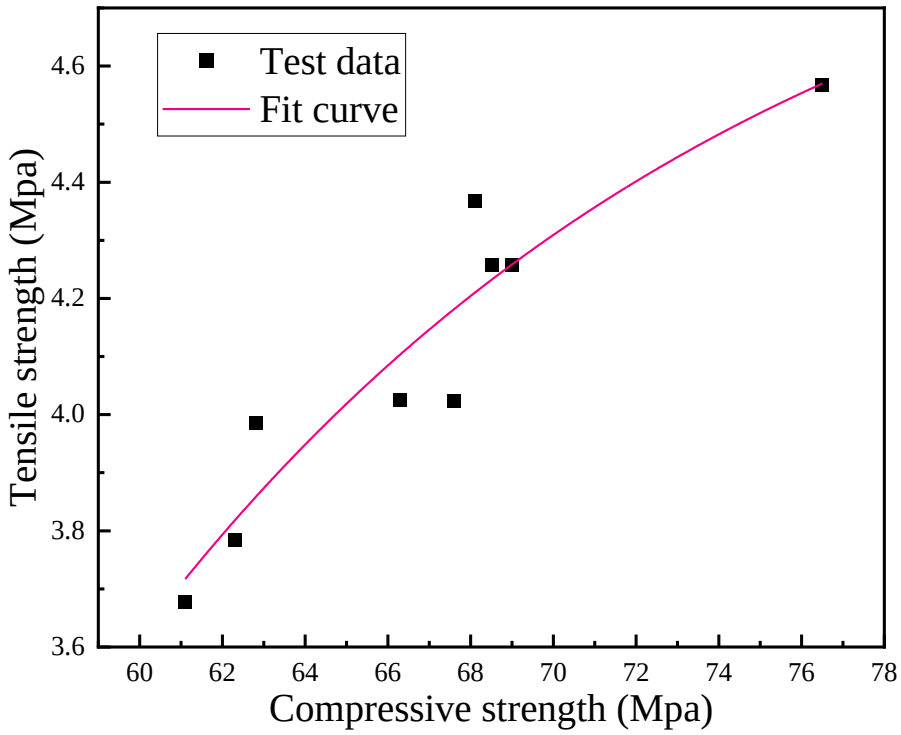

Figure 16. Relationship between uniaxial tensile strength and uniaxial cubic compressive strength.

3.2.8. SEM Analysis of Fracture Surfaces of Tensile Specimens

The observed results are shown in Figure 17. Most PP fibers in the specimen have irregular end morphology, and only a few PP fibers adhere to the matrix, while a slight necking phenomenon occurs, as well as the presence of a portion of fibers left behind after being pulled out of the holes. This indicates that when the specimen is damaged, part of the PP fibers will be torn off, and part of them will be pulled out. In RMPB1.5, RMPC1.5, and RMP-PP-ECCD1.5, the surface of the specimen is relatively flat and dense, and the distribution of the hydration product phases is more uniform, with better hydration and a large number of plate-like C-S-H gel and a small number of $CaCO_3$ crystals form a dense cement cementitious gel. These phenomena better illustrate that the admixture of PP fibers improves the internal pore structure of RMP-PP-ECC and prevents the generation or development of microcracks in concrete, thus improving the load-bearing capacity and service life of RMP-PP-ECC. It effectively promoted the hydration of cement, made the hydration product phase of concrete more uniformly dispersed, and optimized the microstructure of concrete. The primary cause of specimen failure lies in the cohesive force between the fibers and the matrix, surpassing the ultimate tensile strength of the fibers [50]. Consequently, upon the occurrence of specimen damage, certain PP fibers will

experience extraction; however, they will retain their ability to function as fiber bridges, thereby controlling crack width. This factor contributes to the PP fibers' enhanced ductility in RMP-PP-ECC. During the stretching process, a limited number of fiber fragments may become visible on the surface of the PP fibers. This occurrence is mostly attributed to the application of a substantial tensile force. As the RMP substitution rate increases, the number of ash particles in the RMP-PP-ECC matrix increases, and the amount of hydration products of cement and ash particles involved in secondary hydration reactions decreases. This ultimately leads to a large number of spherical ash particles in the RMP-PP-ECC matrix, which reaches its most significant level when the RMP substitution rate is 40%. Only part of the RMP can play the role of volcanic ash, and the remaining RMP particles are distributed in the cement particles; the internal lap is extremely loose, and the generation of hydration reaction products observed from the surface of the specimen is small, which fails to play the role of a good filler, and therefore also results in the lower compressive strength of the specimen. It can be seen that when the dosage of RMP increases, the cement hydration is incomplete, the hydration product decreases, and the internal defects of RMP-PP-ECC increase, resulting in a decrease in its strength.

3.2.9. Effect of RMP-PP-ECC on Anti-Chloride Permeation Performance

As shown in Figure 18, the variation in anti-chlorine ion permeation properties of RMP-PP-ECC with different RMP substitution rates when the PP content is 0%. With the increase in fiber doping of the RMP substitution rate, the electrical flux of the RMP-PP-ECC exhibits a trend characterized by a gradual decline followed by a subsequent increase. In the RMP with the substitution rate of 10%, the electrical flux of the RMP-PP-ECCB0 is observed to exhibit a reduction of 10.3% when compared to the baseline group, when the RMP substitution rate of 10%, 20%, 30%, and 40%, the electric flux exhibits an initial increase followed by a subsequent drop upon the introduction of fiber doping, the rise in electric flux is more pronounced when the RMP substitution rate exceeds 30%. The reason is similar to the mechanical properties, which is due to the uneven particle size of the RMP particles and the increase in the amount of water required to keep the mortar with a certain degree of fluidity. Furthermore, RMP contains elevated levels of alkaline substances, and its volcanic ash effect occurs in alkaline environments. The resultant C-S-H gel can effectively occupy internal voids within RMP-PP-ECC, enhancing its microporous structure. Meanwhile, the non-reactive particles in RMP act as minuscule aggregates, filling the cement mortar matrix. Therefore, when the RMP substitution rate is low, it is favorable to improve the performance of RMP-PP-ECC against chloride ion erosion. However, when the RMP substitution rate is greater than 30%, RMP adversely affects the chloride erosion resistance of RMP-PP-ECC due to the uneven particle size of the RMP particles and the increase in the amount of water required to keep the mortar with a certain degree of fluidity. With an increasing RMP substitution rate, the low reactivity of RMP-PP-ECC results in a reduction in hydration products, leading to an increase in porosity and microcracks within RMP-PP-ECC. Correspondingly, the cement content in RMP decreases. Furthermore, the decrease in C-S-H gel content in the hydration products also contributes to a decline in the chloride ion resistance performance of RMP-PP-ECC. When the RMP substitution rate is 10% and PP content is 1.5%, the electric flux is the smallest, which is decreased by 56.3% compared to the control group. This is because due to the smooth surface of PP, the internal structure of the fiber combined with the fiber reduces the permeability by preventing the expansion of the tiny cracks, and the impregnating medium can not penetrate into the interior of the fibers, which reduces the degree of deterioration of the RMP-PP-ECC specimen, PP reduces the permeability by preventing the expansion of the tiny cracks. PP reduces permeability by preventing the expansion of tiny cracks [51,52].

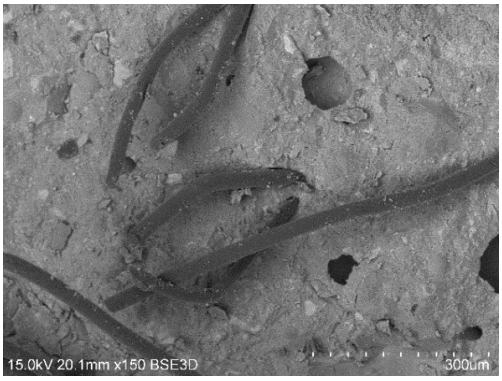

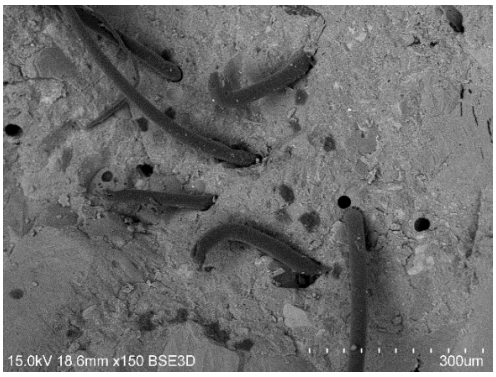

(**a**) RMP-PP-ECCB1.5

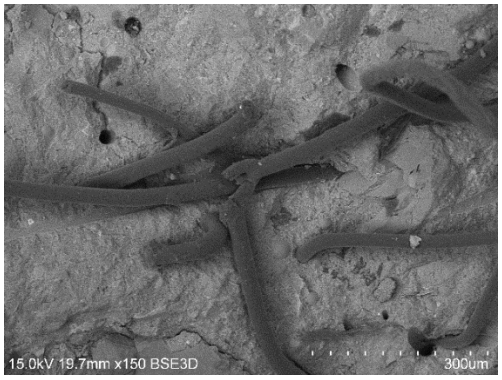

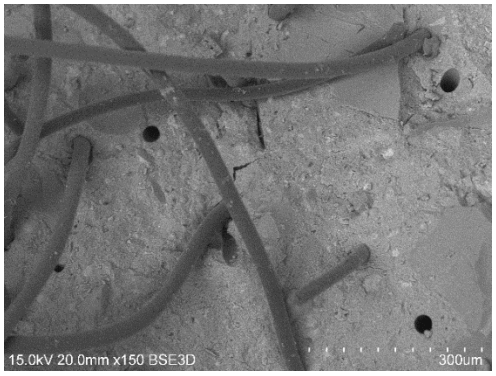

(**b**) RMP-PP-ECCC1.5

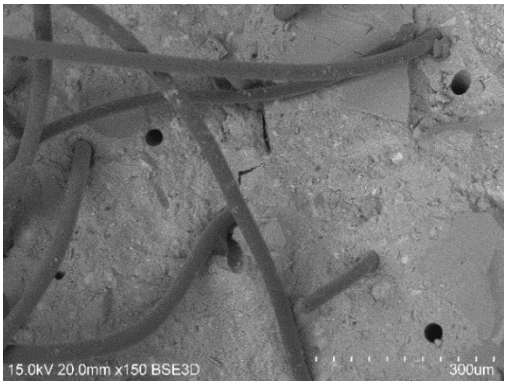

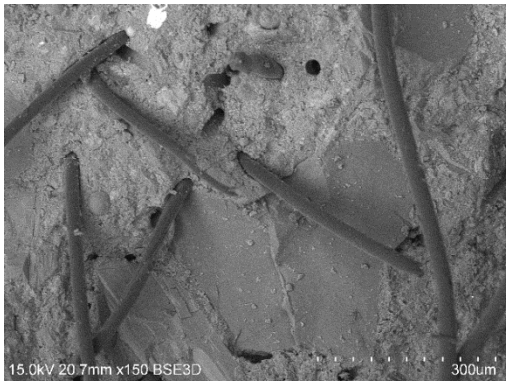

(**c**) RMP-PP-ECCD1.5

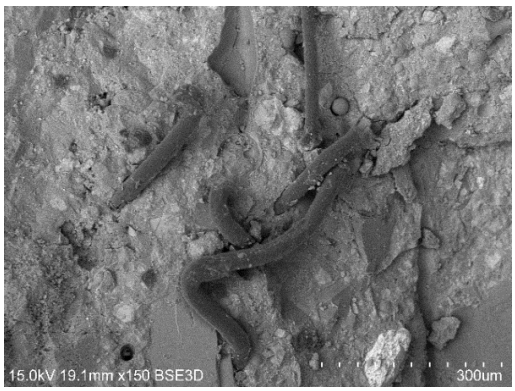

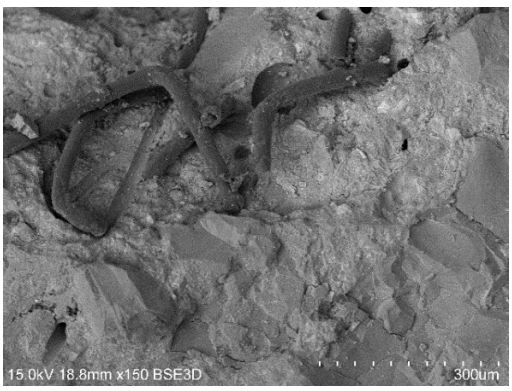

(**d**) RMP-PP-ECCE1.5

Figure 17. SEM of RMP-PP-ECC tensile block fracture surface.

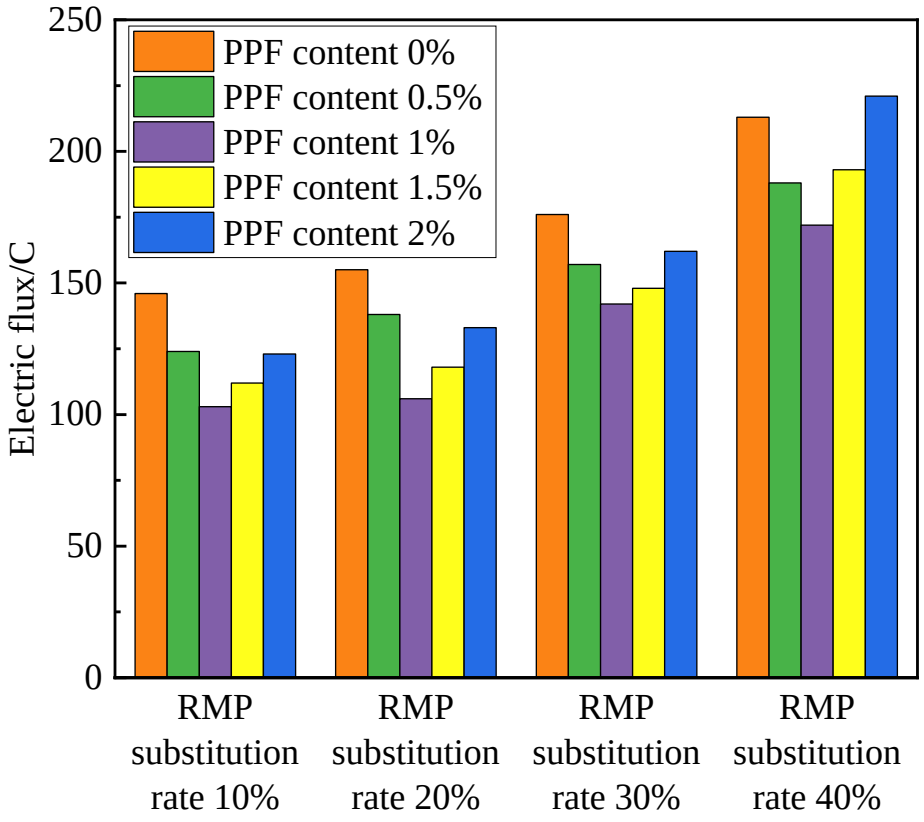

(**a**) RRMP-PP-ECCB0-RMP-PP-ECCE2

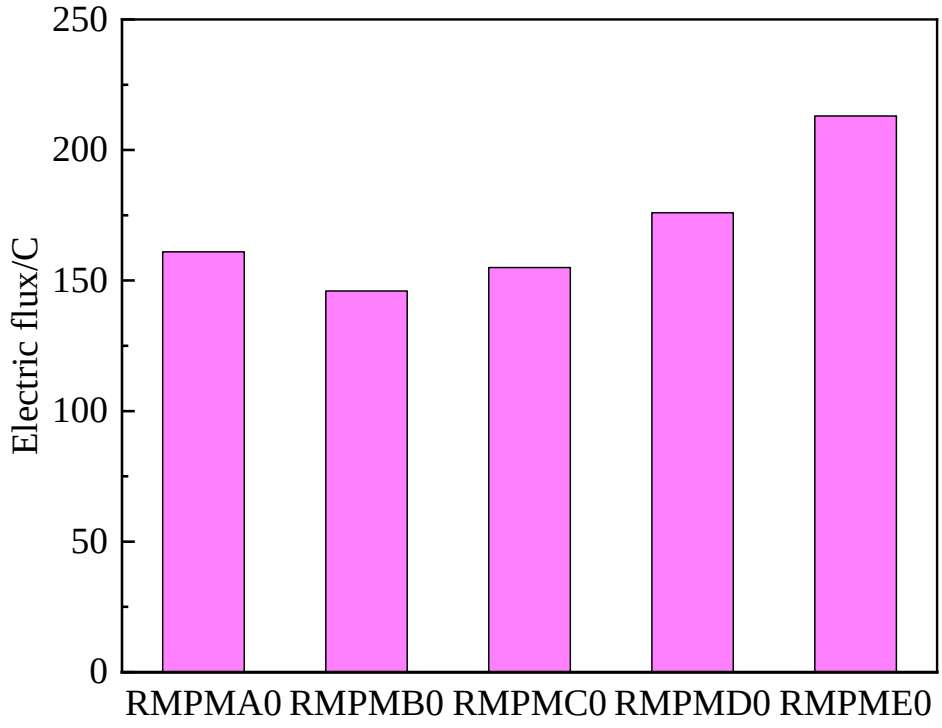

(**b**) Electrical flux in the fiberless group

Figure 18. Chloride ion penetration resistance of RMP-PP-ECCs.

3.2.10. Effect of RMP-PP-ECC on Resistance to Freeze–Thaw Performance

As shown in Figure 19, the effect of freeze–thaw cycles of 0, 25, 50, 75, 100, 125, and 150 times on the RMP-PP-ECCB1.5 specimens' resistance to freeze–thaw damage is

illustrated. After 75 freeze–thaw cycles, on the specimen surface, there is a small amount of mortar fall off, there is a little bit of fiber precipitation, and a small number of small cracks and holes can be observed; the damage on the surface of the RMP-PP-ECC is relatively small, and a slight slagging appeared in part of the area. After 100 cycles of freezing and thawing, the surface of the RMP-PP-ECC specimen exhibits extensive mortar spalling, numerous microvoids, and a small number of missing corners; the degree of damage is more serious, a serious slagging and shedding phenomenon has appeared in the surface area. After 150 freeze–thaw cycles, the phenomenon of mortar shedding is further aggravated, a large number of corners are missing, and the holes have also further expanded. The freeze–thaw damage of the specimens was so severe that significant slagging and shedding had occurred in the surface area. When conducting rapid freeze–thaw experiments, the internal structure of RMP-PP-ECC will be damaged to a certain extent after a certain number of freeze–thaw cycles. Therefore, by analyzing the mass-loss rate of RMP-PP-ECC, the freeze–thaw durability performance of RMP-PP-ECC can be effectively evaluated. Figure 20 shows the mass-loss rate of RMP-PP-ECC under different numbers of freeze–thaw cycles. It can be seen that when the number of freeze–thaw cycles is 0–50 times, the mass of RMP-PP-ECC doped with PP increases. The reason for this is that firstly, as the temperature decreases, the specimen freezes in the water retention state, and the freezing and expanding force generated when the water freezes into ice squeezes the unfrozen water in the capillary pores out of the gel and transports this water into the crystals in the pores, which causes these crystals to grow continuously, resulting in the generation of micro-cracks in the organism. Additionally, with the breaking of the freeze–thaw cycle, the PP fiber is exposed to the microcracks in the specimen. During the process of thawing, it also absorbs the surrounding water through capillary adsorption, such that the quality of the specimen increases. With the increase in the number of freeze–thaw cycles, the water molecules in the RMP-PP-ECC began to be saturated and, after much reciprocal freezing, produced stress, which in turn caused freeze–thaw cycle damage inside the RMP-PP-ECC resulting in the phenomenon of slagging and peeling off the surface of the RMP-PP-ECC and the gradual decrease in the mass of the specimen. As the number of freeze–thaw cycles continued to increase, the freeze–thaw damage accumulated, resulting in a gradual increase in the rate of mass loss of the RMP-PP-ECC soil. RMP-PP-ECCB0 performed the best among the non-fiber-reinforced specimens with 0.044% mass loss after 50 cycles and 0.16% mass loss after 150 cycles, and RMP-PP-ECCB1 performed the best among all the specimens with 0.031% mass gain after 50 cycles and 0.13% mass loss after 150 cycles.

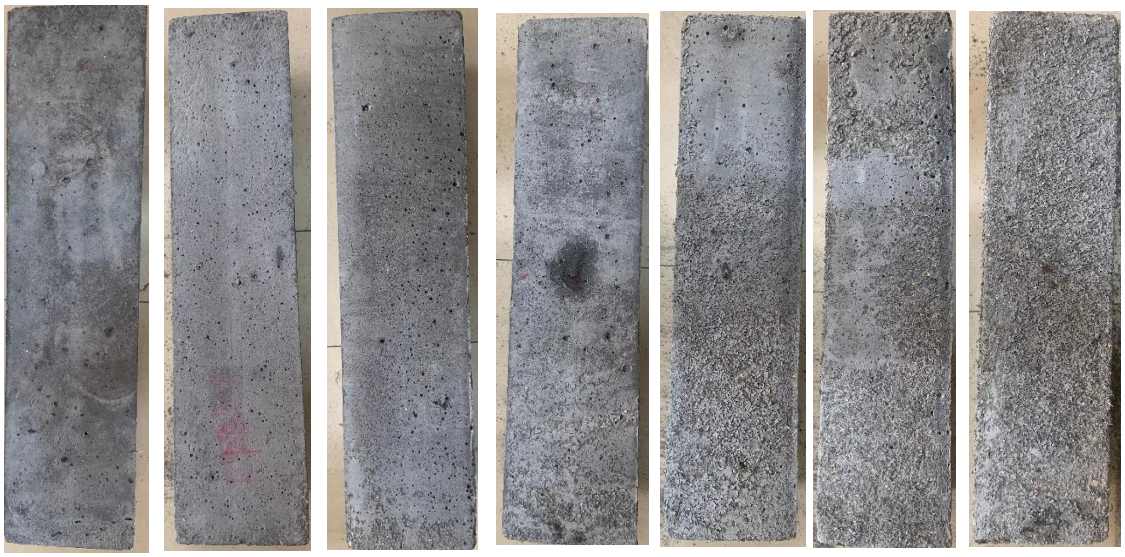

(**a**) 0 (**b**) 25 (**c**) 50 (**d**) 75 (**e**) 100 (**f**) 125 (**g**) 150

Figure 19. Damage condition of RMP-PP-ECC under different freeze–thaw cycles.

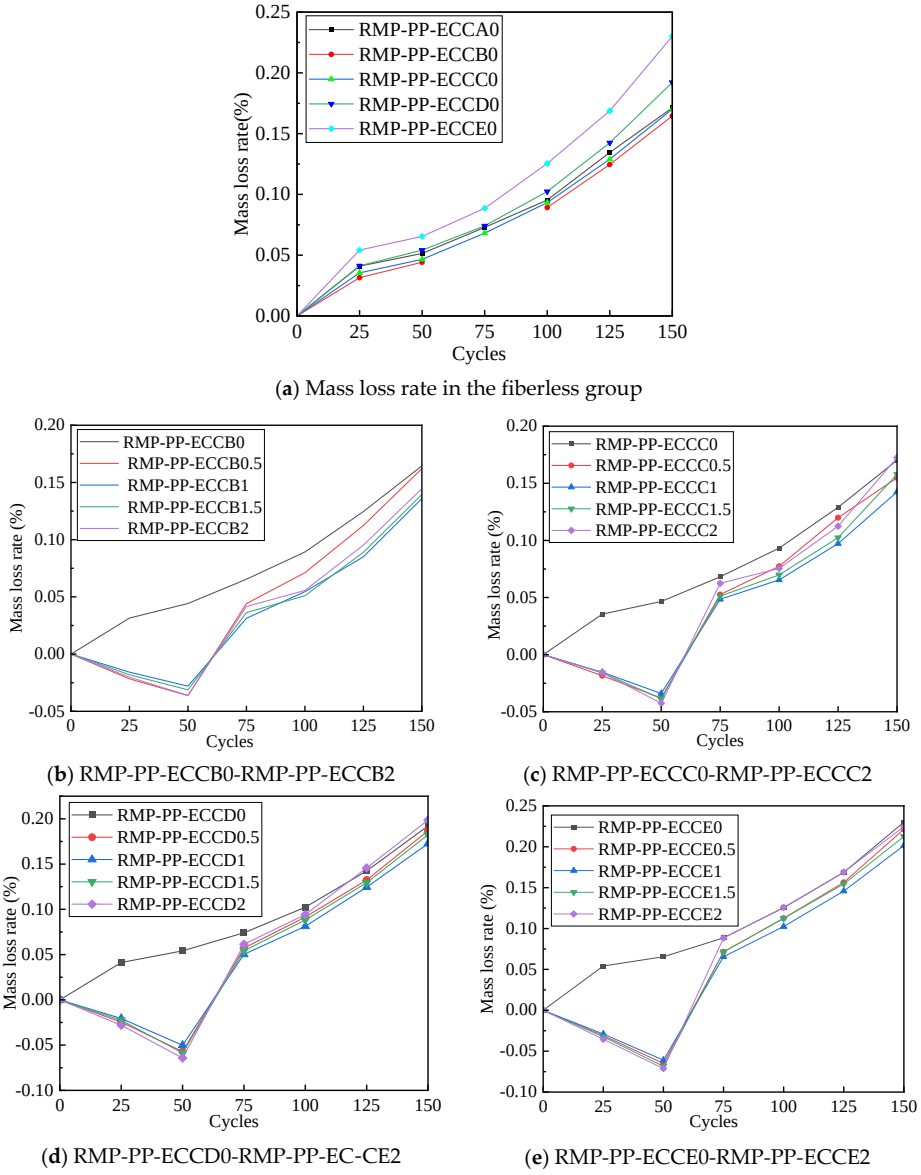

(**a**) Mass loss rate in the fiberless group

(**b**) RMP-PP-ECCB0-RMP-PP-ECCB2

(**c**) RMP-PP-ECCC0-RMP-PP-ECCC2

(**d**) RMP-PP-ECCD0-RMP-PP-EC-CE2

(**e**) RMP-PP-ECCE0-RMP-PP-ECCE2

Figure 20. Mass-loss rate of RMP-PP-ECCs.

As Figure 21 shows, the changes in the relative dynamic elastic modulus of RMP-PP-ECC under different numbers of freeze–thaw cycles, it is obvious from the figure that the relative dynamic elastic modulus of RMP-PP-ECC decreases continuously with the gradual increase in the number of freeze–thaw cycles. In addition, the relative dynamic elastic modulus of RMP-PP-ECC shows a tendency to increase and then decrease with the gradual increase in RMP substitution rate and fiber content. Among the specimens without fiber doping, RMP-PP-ECCB0 has the best performance, with the relative dynamic elastic modulus decreasing by 3.9% after 50 freeze–thaw cycles and the relative dynamic elastic modulus decreasing by 17.9% after 150 freeze–thaw cycles. RMP-PP-ECCB1 showed the best performance among all the specimens, with a decrease of 1.4% after 50 freeze–thaw cycles and a decrease of 15.2% after 150 freeze–thaw cycles. The effect of the change in RMP substitution rate on the frost resistance of RMP-PP-ECC was analyzed: when RMP replaced part of the cement material, the amount of cement used was reduced, and the amount of unhydrated cementitious material was reduced when it entered the hydration stage. Due to the small particle size of RMP, it can be uniformly distributed in the cement paste after replacing cement in appropriate amounts, which not only can become the core of hydration products but also can effectively fill the pores and micro-defects in RMP-

PP-ECC, thus improving the pore structure and densification of RMP-PP-ECC. This can reduce the entry of environmental water molecules and thus improve the frost resistance of RMP-PP-ECC. At the same time, PP demonstrates hydrophilicity and good bonding with cementitious materials, which can reduce the shrinkage cracks produced by mortar in the process of early maintenance, reduce the cracks produced by the shrinkage of mortar in the process of freezing and thawing repeatedly, and inhibit the development of cracks to increase the toughness of the specimen in the process of freezing and thawing repeatedly; on the other hand, the mixing of PP reduces the internal pore space in the RMP-PP-ECC, reduces the freezing point of the pore space, and thus improves the frost resistance of RMP-PP-ECC [40,53–55].

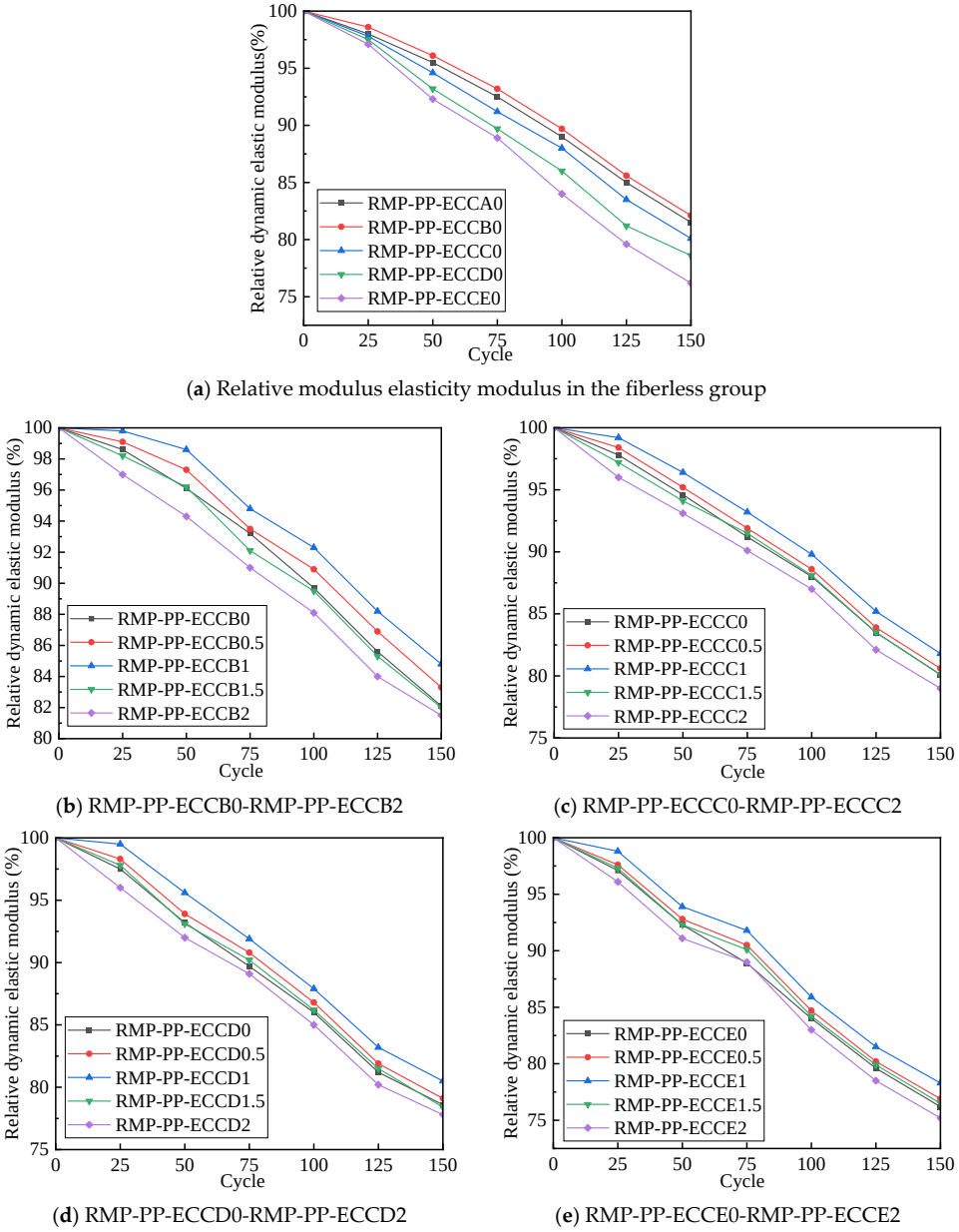

(**a**) Relative modulus elasticity modulus in the fiberless group

(**b**) RMP-PP-ECCB0-RMP-PP-ECCB2

(**c**) RMP-PP-ECCC0-RMP-PP-ECCC2

(**d**) RMP-PP-ECCD0-RMP-PP-ECCD2

(**e**) RMP-PP-ECCE0-RMP-PP-ECCE2

Figure 21. Relative modulus elasticity modulus of RMP-PP-ECCs.

4. Conclusions

In this study, a comprehensive experiment was conducted to investigate the effect of RMP and PP fibers on the mechanical and durability properties of engineered cementitious composites, and the following conclusions were drawn:

1. According to the XRD and SEM results, the main components in RMP are sand (SiO_2) and calcite ($CaCO_3$) in concrete. The relatively high content of SiO_2 in RMP after ball milling has potential activation properties. The hydration products in the matrix are dense around the fibers, filling the pores within the matrix and inducing the fibers and the matrix to cement each other, thus subjecting the matrix to anisotropic deformation constraints, and the addition of fibers enhances the stability of the matrix, thereby improving the mechanical properties and durability.
2. In cementitious composites, the optimal content for replacing cement with RMP is about 10%; the appropriate amount of RMP can promote the production of C-S-H gel and fill the internal pores of the material to improve the friction between the fibers and the matrix. The RMP should not be too large, the fineness of recycled micronized powder should be fine, and the specific surface area should be large; too much recycled micropowder will lead to increased water demand and incomplete hydration, resulting in reduced mechanical and durability properties. The doping of RM should not be too large, the fineness of recycled micropowder should be fine, and the specific surface area should be large; excessive recycled micropowder doping will lead to increased water demand and incomplete hydration, resulting in a decrease in mechanical and durability properties.
3. The effects of PP fiber on the engineered cementitious composites' flexural and tensile properties, ductility, resistance to chlorine ion penetration, and anti-freezing performance enhancement are more obvious, mainly due to the bridging effect of the fiber, which absorbs part of the external load, slowing down the rate of expansion of cracks. At the same time, the best volume of PP fiber doping should be maintained at 1–1.5%, as excessive PP fiber doping leads to easy adhesion during the mixing and processing of engineered cementitious composites, resulting in a larger fiber-specific surface area and a specimen containing more weak layers, which destroys the optimal structure of the specimen.
4. The compressive strength of RMP-PP-ECB1.5 was increased by 18.8%, the tensile strength performance was increased by 80.8%, and the maximum tensile strain was increased by 314% compared with the ordinary cementitious composites. The flexural performance of RMP-PP-ECCB1 was the best, and the flexural strength was increased by 22% compared with that of ordinary cementitious composites. The electric flux of RMP-PP-ECCB1.5 was decreased by 56.3% compared with that of ordinary cementitious composites, the mass-loss rate was reduced by 26% after 150 cycles of freeze–thaw cycle, and the relative mass-loss rate was reduced by 26% compared with that of ordinary cementitious composites. The electrical flux of RMP-PP-ECCB decreased by 56.3% compared to ordinary cementitious composites, the mass-loss rate of RMP-PP-ECCB decreased by 26% compared to ordinary cementitious composites after 150 freeze–thaw cycles, and the relative kinetic elasticity modulus was improved by 4%; the lack of a significant decrease in relative kinetic elasticity modulus indicates that there is no significant change in the internal structure of the material.

Author Contributions: L.Z.: data curation, Formal analysis, investigation, validation, writing-original draft. J.Z.: conceptualization, supervision, project administration. All authors have read and agreed to the published version of the manuscript.

Funding: This research received no external funding.

Data Availability Statement: All experimental data in this paper have been displayed in the Table of the paper.

Conflicts of Interest: The authors declare no conflict of interest.

References

1. Dou, X.; Ma, X.; Zhao, C.; Li, J.; Yan, Y.; Zhu, J. Risk assessment of soil erosion in Central Asia under global warming. *Catena* **2022**, *212*, 106056. [CrossRef]
2. Lin, C.H.; Lai, C.H.; Wu, Y.L.; Chen, M.J. Simple model for estimating dry deposition velocity of ozone and its destruction in a polluted nocturnal boundary layer. *Atmos. Environ.* **2010**, *44*, 4364–4371. [CrossRef]
3. Mandal, S.; Islam, M.S.; Biswas MH, A.; Akter, S. A Mathematical Model Applied to Investigate the Potential Impact of Global Warming on Marine Ecosystems. *Appl. Math. Model.* **2021**, *101*, 19–37. [CrossRef]
4. Xu, D.; Wang, Y.; Wang, Z. Linking priority areas and land restoration options to support desertification control in northern China. *Ecol. Indic.* **2022**, *137*, 108747. [CrossRef]
5. Wang, H.; Wang, L.; Shen, W.; Cao, K.; Sun, L.; Wang, P.; Cui, L. Compressive Strength, Hydration and Pore Structure of Alkali-Activated Slag Mortars Integrating with Recycled Concrete Powder as Binders. *KSCE J. Civ. Eng.* **2022**, *26*, 795–805. [CrossRef]
6. Huang, B.; Wang, X.; Kua, H.; Geng, Y.; Bleischwitz, R.; Ren, J. Construction and demolition waste management in China through the 3R principle. *Resources. Conserv. Recycl.* **2018**, *129*, 36–44. [CrossRef]
7. Meng, T.; Hong, Y.; Ying, K.; Wang, Z. Comparison of technical properties of cement pastes with different activated recycled powder from construction and demolition waste. *Cem. Concr. Compos.* **2021**, *120*, 104065. [CrossRef]
8. Schoon, J.; De Buysser, K.; Van Driessche, I.; De Belie, N. Fines extracted from recycled concrete as alternative raw material for Portland cement clinker production. *Cem. Concr. Compos.* **2015**, *58*, 70–80. [CrossRef]
9. Chang, H.; Wang, X.; Wang, Y.; Li, S.; Wang, J.; Liu, J.; Feng, P. Influence of low vacuum condition on mechanical performance and microstructure of hardened cement paste at early age. *Constr. Build. Mater.* **2022**, *346*, 128358. [CrossRef]
10. Lyu, K.; Garboczi, E.J.; Gao, Y.; Miao, C.; Liu, X. Relationship between fine aggregate size the air void system of six mortars:, I. Air void and diameter distribution. *Cem. Concr. Compos.* **2022**, *131*, 104599. [CrossRef]
11. Cai, R.; Tian, Z.; Ye, H.; He, Z.; Tang, S. The role of metakaolin in pore structure evolution of Portland cement pastes revealed by an impedance approach. *Cem. Concr. Compos.* **2021**, *119*, 103999. [CrossRef]
12. Shagñay, S.; Bautista, A.; Donaire, J.; Torres-Carrasco, M.; Bastidas, D.M.; Velasco, F. Chloride-induced corrosion of steel reinforcement in mortars manufactured with alternative environmentally-friendly binders. *Cem. Concr. Compos.* **2022**, *130*, 104557. [CrossRef]
13. Tan, H.; Du, C.; He, X.; Li, M.; Zhang, J.; Zheng, Z.; Su, Y.; Yang, J.; Deng, X.; Wang, Y. Enhancement of compressive strength of high-volume fly ash cement paste by wet grinded cement: Towards low carbon cementitious materials. *Constr. Build. Mater.* **2022**, *323*, 126458. [CrossRef]
14. Tang, S.; Huang, D.; He, Z. A review of autogenous shrinkage models of concrete. *J. Build. Eng.* **2021**, *44*, 103412. [CrossRef]
15. Cheng, X. Research status and application of reclaimed concrete powder. *Cryog. Build. Technol.* **2009**, *31*, 78–79.
16. Kim, Y.J.; Choi, Y.W. Utilization of waste concrete powder as a substitution material for cement. *Constr. Build. Mater.* **2012**, *30*, 500–504. [CrossRef]
17. Zhang, D.; Zhang, S.; Huang, B.; Yang, Q.; Li, J. Comparison of mechanical, chemical, and thermal activation methods on the utilisation of recycled concrete powder from construction and demolition waste. *J. Build. Eng.* **2022**, *61*, 105295. [CrossRef]
18. Tang, Q.; Ma, Z.; Wu, H.; Wang, W. The utilization of eco-friendly recycled powder from concrete and brick waste in new concrete: A critical review. *Cem. Concr. Compos.* **2020**, *114*, 103807. [CrossRef]
19. Mao, X.; Qu, W.; Zhu, P. Mixture Optimization of Green Reactive Powder Concrete with Recycled Powder. *J. Mater. Civ. Eng.* **2019**, *31*, 04019033. [CrossRef]
20. Yu, K.-Q.; Zhu, W.-J.; Ding, Y.; Lu, Z.-D.; Yu, J.-T.; Xiao, J.-Z. Micro-structural and mechanical properties of ultra-high performance engineered cementitious composites (UHP-ECC) incorporation of recycled fine powder (RFP). *Cem. Concr. Res.* **2019**, *124*, 105813. [CrossRef]
21. Ji, J.; Song, H.; Jiang, L.; Ren, H.; Zhang, Y.; Liu, Y. Tensile Performance of High Ductility Cementitious Composites With Recycled Powder From C&D Waste. *Front. Mater.* **2021**, *8*, 673752.
22. Wu, R.; Zhao, T.; Zhang, P.; Yang, D.; Liu, M.; Ma, Z. Tensile Behavior of Strain Hardening Cementitious Composites (SHCC) Containing Reactive Recycled Powder from Various C&D Waste. *J. Renew. Mater.* **2021**, *9*, 743.
23. Likes, L.; Markandeya, A.; Haider, M.M.; Bollinger, D.; McCloy, J.S.; Nassiri, S. Recycled concrete and brick powders as supplements to Portland cement for more sustainable concrete. *J. Clean. Prod.* **2022**, *364*, 132651. [CrossRef]
24. Khan, Q.S.; Sheikh, M.N.; McCarthy, T.J.; Robati, M.; Allen, M. Experimental investigation on foam concrete without and with recycled glass powder: A sustainable solution for future construction. *Constr. Build. Mater.* **2019**, *201*, 369–379. [CrossRef]
25. Zhou, C.S.; Ji, H.B.; Zhao, L.Y. Application and Research Progress of Recycled Micro-powders in Cement-Based Materials. *Bull. Chin. Ceram. Soc.* **2019**, *38*, 2456–2463.
26. Guo, Q.; Li, X.; Wang, S. Experimental study on workability and compressive properties of fiber reinforced recycled powder concrete. *Concrete* **2022**, 109–112.
27. Mechanical Property of Recycled Micro-powder Cementitious Composites with Ultra-high Ductility. *Mater. Rep.* **2019**, *33*, 1328–1334.

28. Ye, J.; Cui, C.; Yu, J.; Yu, K.; Xiao, J. Fresh and anisotropic-mechanical properties of 3D printable ultra-high ductile concrete with crumb rubber. *Compos. Part B Eng.* **2021**, *211*, 108639. [CrossRef]
29. Cai, Z.; Liu, F.; Yu, J.; Yu, K.; Tian, L. Development of ultra-high ductility engineered cementitious composites as a novel and resilient fireproof coating. *Constr. Build. Mater.* **2021**, *288*, 123090. [CrossRef]
30. Zhang, W.; Deng, M.; Han, Y.; Li, R.; Yang, S. Uniaxial tensile performance of high ductile fiber-reinforced concrete with built-in basalt textile grids. *Constr. Build. Mater.* **2022**, *315*, 125716. [CrossRef]
31. Yang, K.; He, Z.; Li, D.; Xu, H.; Kong, L. Experimental Study on Basalt Fiber Crack Resistance of Asphalt Concrete Based on Acoustic Emission. *Materials* **2021**, *14*, 4096. [CrossRef] [PubMed]
32. Shang, X.-Y.; Yu, J.-T.; Li, L.-Z.; Lu, Z.-D. Shear strengthening of fire damaged RC beams with stirrup reinforced engineered cementitious composites. *Eng. Struct.* **2020**, *210*, 110263. [CrossRef]
33. *GB/T 50081-2019*; Ministry of Housing and Urban-Rural Development of the People's Republic of China. The Standard for Test Methods of Concrete Physicaland Mechanical Properties. China Architecture & Building Press: Beijing, China, 2019. (In Chinese)
34. *GB/T 50082-2009*; Ministry of Housing and Urban-Rural Development of the People's Republic of China. Standard for Test Methods of Long-Term Performance and Durability of Ordinary Concrete. China Architecture & Building Press: Beijing, China, 2009. (In Chinese)
35. Korf, N.; Løvik, A.N.; Figi, R.; Schreiner, C.; Kuntz, C.; Mählitz, P.M.; Rösslein, M.; Wäger, P.; Rotter, V.S. Multi-element chemical analysis of printed circuit boards –challenges and pitfalls. *Waste Manag.* **2019**, *92*, 124–136. [CrossRef]
36. Gencel, O.; Erdugmus, E.; Sutcu, M.; Oren, O.H. Effects of concrete waste on characteristics of structural fired clay bricks. *Constr. Build. Mater.* **2020**, *255*, 119362. [CrossRef]
37. Dong, Y.; Xiao, K.T.; Yang, H.Q. Influence of Limestone Powder on the Performance of Cementitious Materials. *Appl. Mech. Mater.* **2014**, *541–542*, 123–129. [CrossRef]
38. Shi, C.J.; Wang, D.H.; Jia, H.F.; Liu, J.H. Role of Limestone Powder and Its Effect on Durability of Cement-Based Materials. *J. Chin. Ceram. Soc.* **2017**, *45*, 1582–1593.
39. Yusuf, S.M.; Choo, E.; Gao, N. Comparison between Virgin and Recycled 316L SS and AlSi10Mg Powders Used for Laser Powder Bed Fusion Additive Manufacturing. *Metals* **2020**, *10*, 1625. [CrossRef]
40. Gao, Y.; Cui, X.; Lu, N.; Hou, S.; He, Z.; Liang, C. Effect of recycled powders on the mechanical properties and durability of fully recycled fiber-reinforced mortar. *J. Build. Eng.* **2022**, *45*, 103574. [CrossRef]
41. Xu, J.; Kang, A.; Wu, Z.; Gong, Y.; Xiao, P. The effect of mechanical-thermal synergistic activation on the mechanical properties and microstructure of recycled powder geopolymer. *J. Clean. Prod.* **2021**, *327*, 129477. [CrossRef]
42. Liu, S.; Yan, P. Effect of Limestone Powder on Microstructure of Concrete. *Wuhan Univ. Technol. J. Mater. Sci.* **2010**, *25*, 328–331. [CrossRef]
43. Kim, J.; Jang, H. Closed-loop recycling of C&D waste: Mechanical properties of concrete with the repeatedly recycled C&D powder as partial cement replacement. *J. Clean. Prod.* **2022**, *343*, 130977. [CrossRef]
44. Yuan, C.; Chen, Y.; Liu, D.; Lv, W.; Zhang, Z. The basic mechanical properties shrinkage properties of recycled micropowder, U.H.P.C. *Materials* **2023**, *16*, 1570. [CrossRef]
45. Wang, X.; Yan, Y.; Tong, X.; Gong, Y. Investigation of Mineral Admixtures on Mechanical Properties of Alkali-Activated Recycled Concrete Powders Cement. *Buildings* **2022**, *12*, 1234. [CrossRef]
46. Sharaky, I.A.; Elamary, A.S.; Alharthi, Y.M. Effect of Waste Basalt Fines and Recycled Concrete Components on Mechanical, Water Absorption, and Microstructure Characteristics of Concrete. *Materials* **2022**, *15*, 4385. [CrossRef]
47. Zhao, G.; Zhu, Z.; Ren, G.; Wu, T.; Ju, P.; Ding, S.; Shi, M.; Fan, H. Utilization of recycled concrete powder in modification of the dispersive soil: A potential way to improve the engineering properties. *Constr. Build. Mater.* **2023**, *389*, 131626. [CrossRef]
48. Bonavetti, V.; Rahhal, V.; Irassar, E. Studies on the carboaluminate formation in limestone filler-blended cements. *Cem. Concr. Res.* **2001**, *31*, 853–859. [CrossRef]
49. Xiao, J.; Ma, Z.; Sui, T.; Akbarnezhad, A.; Duan, Z. Mechanical properties of concrete mixed with recycled powder produced from construction and demolition waste. *J. Clean. Prod.* **2018**, *188*, 720–731. [CrossRef]
50. Song, S.; Li, X.; Wang, Z.; Wang, W. Orthogonal experimental and theoretical study on mechanical properties of fiber-reinforced recycled powder concrete. *Case Stud. Constr. Mater.* **2022**, *17*, e01546. [CrossRef]
51. Sun, C.; Chen, L.; Xiao, J.; Singh, A.; Zeng, J. Compound utilization of construction and industrial waste as cementitious recycled powder in mortar. *Resour. Conserv. Recycl.* **2021**, *170*, 105561. [CrossRef]
52. Wang, Y.; Liu, Z.; Wang, Y.; Li, Q.; Gong, X.; Zhao, Y. Effect of recycled aggregate and supplementary cementitious material on mechanical properties and chloride permeability of concrete. *J. Clean. Prod.* **2022**, *369*, 133322. [CrossRef]
53. Zhou, L.A.; Liu, Y.; Lu, J.; Zhou, W.; Wang, H. Influence of recycled concrete powder (RCP) and recycled brick powder (RBP) on the physical/mechanical properties and durability of raw soil. *Coatings* **2021**, *11*, 1475. [CrossRef]

54. Kuranlı, F.; Uysal, M.; Abbas, M.T.; Çoşgun, T.; Niş, A.; Aygörmez, Y.; Canpolat, O.; Al-Mashhadani, M.M. Mechanical and durability properties of steel, polypropylene and polyamide fiber reinforced slag-based alkali-activated concrete. *Eur. J. Environ. Civ. Eng.* **2022**, *27*, 114–139. [CrossRef]
55. Yao, Y.; Liu, C.; Liu, H.; Zhang, W.; Hu, T. Deterioration mechanism understanding of recycled powder concrete under coupled sulfate attack and freeze–thaw cycles. *Constr. Build. Mater.* **2023**, *388*, 131718. [CrossRef]